ARTICLES
https://doi.org/10.1038/s41567-021-01474-y

nature physics

Reviving a failed network through microscopic interventions

Hillel Sanhedrai[1], Jianxi Gao[2,3], Amir Bashan[1], Moshe Schwartz[4], Shlomo Havlin[1] and Baruch Barzel[5,6] ✉

From mass extinction to cell death, complex networked systems often exhibit abrupt dynamic transitions between desirable and undesirable states. These transitions are often caused by topological perturbations (such as node or link removal, or decreasing link strengths). The problem is that reversing the topological damage, namely, retrieving lost nodes or links or reinforcing weakened interactions, does not guarantee spontaneous recovery to the desired functional state. Indeed, many of the relevant systems exhibit a hysteresis phenomenon, remaining in the dysfunctional state, despite reconstructing their damaged topology. To address this challenge, we develop a two-step recovery scheme: first, topological reconstruction to the point where the system can be revived and then dynamic interventions to reignite the system's lost functionality. By applying this method to a range of nonlinear network dynamics, we identify the recoverable phase of a complex system, a state in which the system can be reignited by microscopic interventions, for instance, controlling just a single node. Mapping the boundaries of this dynamical phase, we obtain guidelines for our two-step recovery.

Complex systems—biological, social or technological—often experience perturbations and disturbances, from overload failures in power systems[1–3] to species extinction in ecological networks[4–6]. The impact of such perturbations is often subtle: the system exhibits a minor response, but it continues to sustain its global functionality[7,8]. However, in extreme cases, a large enough perturbation may lead to a major collapse, with the system abruptly transitioning from a functional to a dysfunctional dynamic state[9–13] (Fig. 1a–d). When such collapse occurs, the naïve instinct is to reverse the damage, retrieve the failed nodes and reconstruct the lost links. This, however, is seldom efficient because of the following reasons: (1) we rarely have access to all the system components[14], limiting our ability to reconstruct the perturbed network; (2) even if we could reverse the damage, in many cases, the system will not spontaneously regain its lost functionality due to hysteresis.

To address this challenge, here we derive a two-step recovery process. Step I. Restructuring (Fig. 1e). Retrieving the weighted topology to a point where the system can potentially regain its functionality. Step II. Reigniting (Fig. 1f). Introducing dynamic interventions to steer the system back to its functional state. Considering the fact that in most practical scenarios, we cannot control the majority of the system components, we design our reigniting around micro-interventions, that is, controlling only a small number of components. To achieve this, we uncover the recoverable phase—a dynamic state in which the system can be driven towards functionality by controlling just a single node.

Challenge of irreversible collapse

Consider a complex system of N components (nodes), interacting via an adjacency matrix A, a sparse, potentially directed random network with an arbitrary degree distribution $P(k_{\rm in}, k_{\rm out})$ (Supplementary Section 1). Each node is assigned an activity $x_i(t)$, whose meaning depends on context, for example, capturing a species abundance in a microbial network or a gene's expression level in a biological setting. We then track the evolution of $x_i(t)$ following[15–17]

$$\frac{{\rm d}x_i}{{\rm d}t} = M_0(x_i(t)) + \sum_{j=1}^{N} A_{ij} W_{ij} M_1(x_i(t)) M_2(x_j(t)), \qquad (1)$$

where the interaction dynamics is characterized by the three potentially nonlinear functions $M_0(x)$, $M_1(x)$ and $M_2(x)$. The first function, $M_0(x_i)$, captures node i's self-dynamics, describing mechanisms such as protein degradation[18] (cellular), individual recovery[19] (epidemic) or birth/death processes[20] (population dynamics). The product $M_1(x_i)M_2(x_j)$ describes the (i,j) interaction mechanism, for example, genetic activation[21], infection[19] or symbiosis[22]. The strength of the (i,j) interaction is governed by W_{ij}, a random weight extracted from the density function $P(w)$, whose average is denoted by $\omega = \int_0^\infty wP(w){\rm d}w$.

In the context of recoverability, we seek to revive the activity of all the nodes by activating a selected set of nodes; hence, we focus on cooperative interactions in which the nodes positively contribute to each other's activity. This is expressed in equation (1) through $W_{ij}M_1(x_i)M_2(x_j) \geq 0$ (Supplementary Section 1). Later, in our discussion on microbiome recoverability, we relax this condition and examine the impact of mixed-sign interactions.

Setting the derivative on the left-hand side of equation (1) to zero, we obtain the system's fixed points, namely, $\mathbf{x}_\alpha = (x_{\alpha,1}, \ldots, x_{\alpha,N})^\top$, which, if dynamically stable, represent different states (desirable or undesirable) in which the system can naturally reside. Transitions between these states often result from perturbations to A or W, such as node/link deletion or reduction in link weights. When this occurs, it is difficult to reverse the unwanted transition. This is because the system often avoids spontaneous recovery, even if we

[1]Department of Physics, Bar-Ilan University, Ramat-Gan, Israel. [2]Network Science and Technology Center, Rensselaer Polytechnic Institute, Troy, NY, USA. [3]Department of Computer Science, Rensselaer Polytechnic Institute, Troy, NY, USA. [4]Department of Physics, Tel Aviv University, Tel Aviv, Israel. [5]Department of Mathematics, Bar-Ilan University, Ramat-Gan, Israel. [6]Gonda Multidisciplinary Brain Research Center, Bar-Ilan University, Ramat-Gan, Israel. ✉e-mail: baruchbarzel@gmail.com

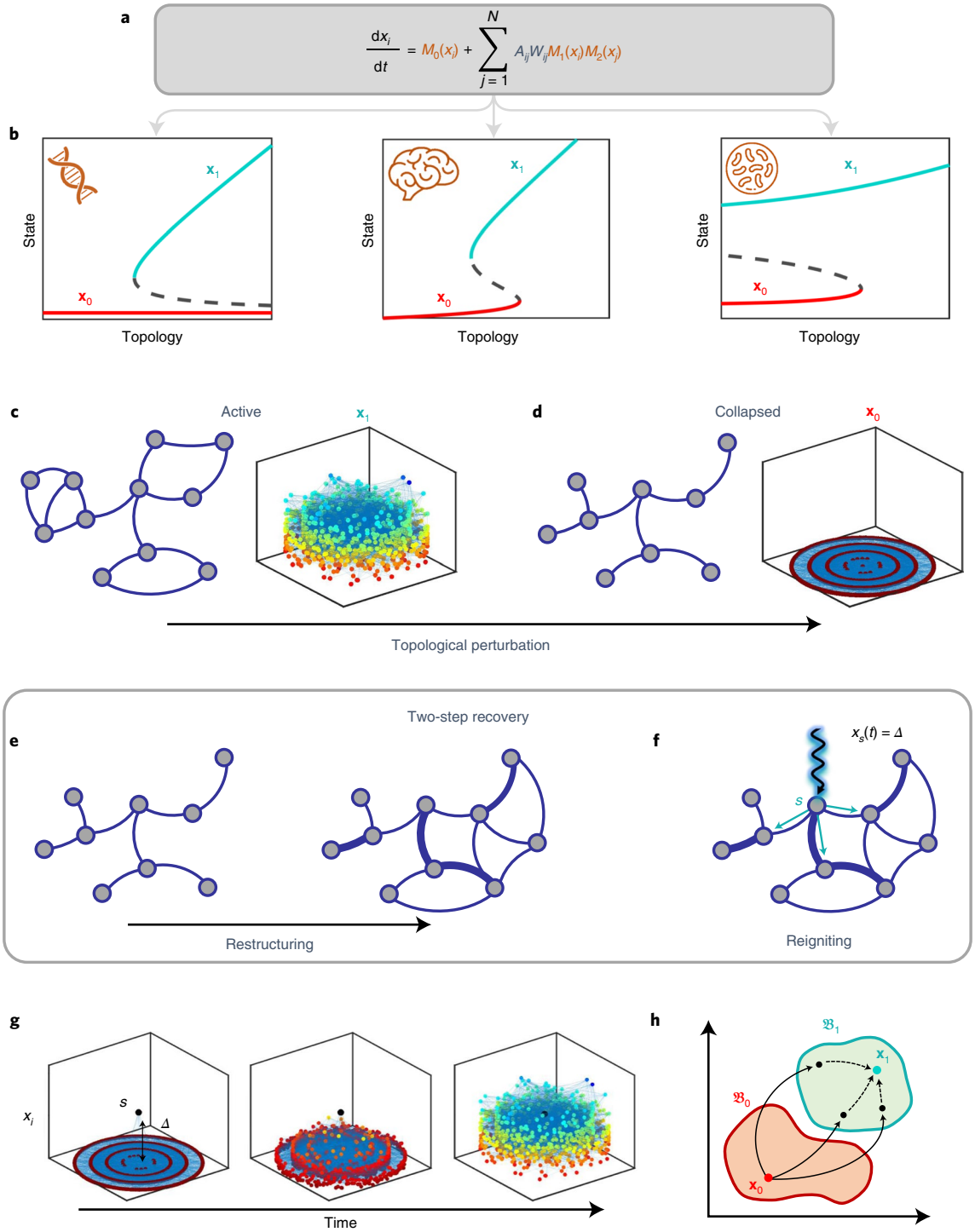

Fig. 1 | Reviving a failed network. a, Components of our modelling framework: network structure/weights are captured by A and W (grey terms); interaction mechanisms are described by $M_0(x)$, $M_1(x)$ and $M_2(x)$ (orange terms). **b**, Depending on the dynamics—for example, cellular, neuronal or microbial—the system exhibits distinct fixed points, active ($\mathbf{x}_1$, green) or failed ($\mathbf{x}_0$, red). Transitions between these states are driven by perturbations to A and W. **c**, Unperturbed, the system resides in $\mathbf{x}_1$, where all $x_i > 0$. In this presentation, here and throughout, the network nodes are laid out on the x–y plane, and their activities x_i are captured by the z coordinate. Hence, an active system has all the nodes spread along the positive z axis, whereas a failed network is laid out around $z \to 0$. We also use colour coding from red (small x_i) to blue (large x_i) as a visual aid. **d**, Perturbations to A and W, such as node/link removal or weight reduction, result in a collapse to the inactive $\mathbf{x}_0$. For this system, under $\mathbf{x}_0$, all the activities vanish ($z = 0$). **e**, Step I. Restructuring. To revive the failed system, we first restructure A and W to a point where it can recover, namely, a point where $\mathbf{x}_1$ is potentially stable. **f**, Step II. Reigniting. After restructuring, we revive the active state $\mathbf{x}_1$ by controlling a microscopic set of nodes (here the single node s). By using an external forcing to sustain constant activity $x_s(t) = \Delta$, we drive the network towards $\mathbf{x}_1$. **g**, Following reigniting ($x_s(t) = \Delta$; black node at the centre), the forcing signal gradually spreads until the system's activity $\mathbf{x}_1$ is restored. **h**, In this process, we use the natural basin structure of our dynamics. To reignite $\mathbf{x}_1$, we steer the system from $\mathfrak{B}_0$ (red) to any point within $\mathfrak{B}_1$ (green). Once in $\mathfrak{B}_1$, we cease our forcing, and the system naturally transitions to the desired $\mathbf{x}_1$ (dashed arrows).

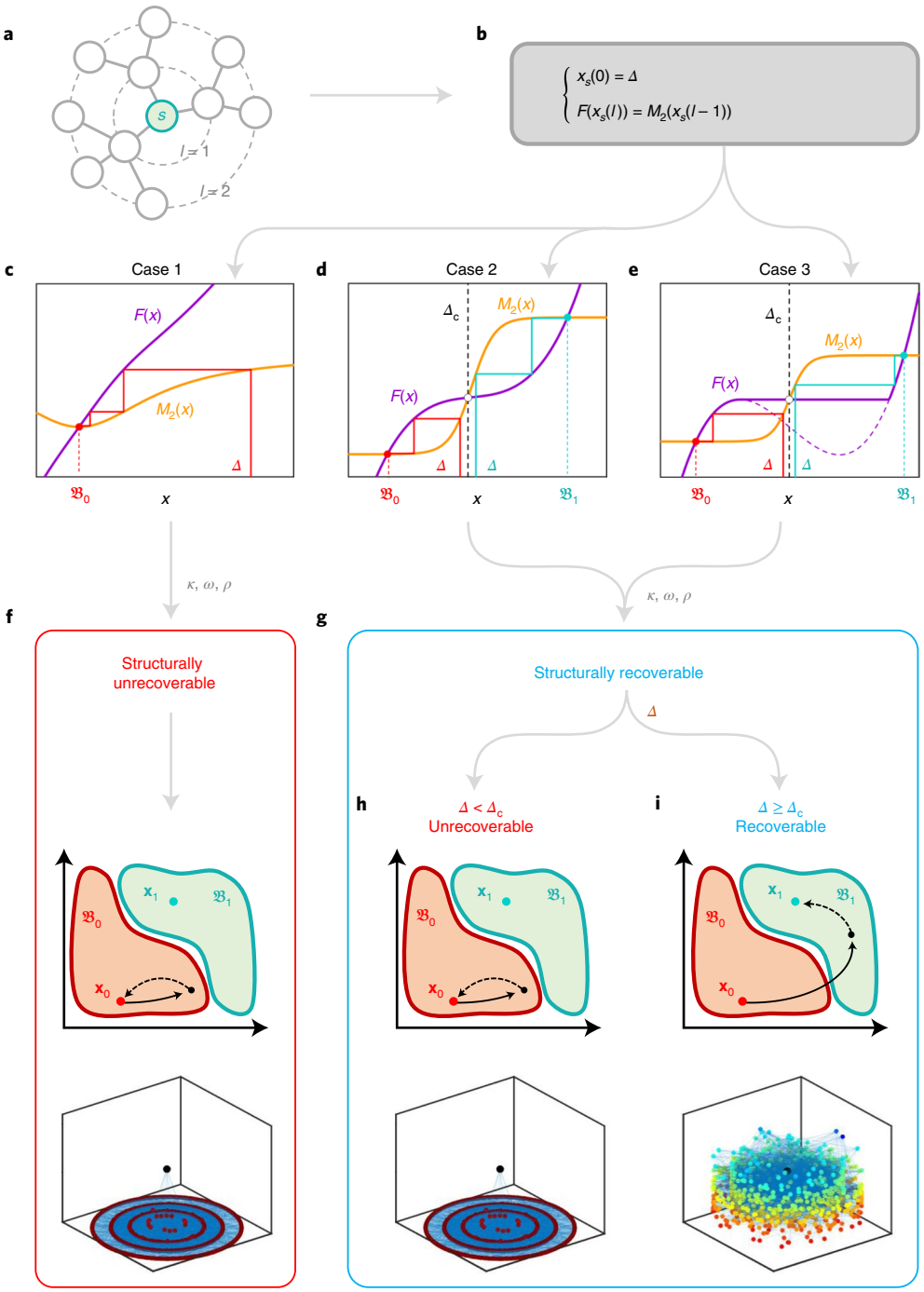

Fig. 2 | Can a system be reignited by a single node? a, During reigniting, we select a single source node *s* and, for a limited time, artificially force it to sustain a permanent activity Δ. To track the system's response, we divide the network into shells $K_s(l)$ comprising all the nodes at distance *l* from *s* **b**, Average activity $x_s(l)$ of all the nodes at $K_s(l)$ follows the recurrence relation of equation (5), starting from our forcing at *s* (top equation) and tracking its propagation as it penetrates the network shells (bottom equation). Successful reigniting requires $x_s(l \to \infty) \in \mathfrak{B}_1$, that is, the distant shells were driven towards the desired basin. **c**–**e**, To track the convergence of the recurrence relation, we plot $F(x)$ (purple) and $M_2(x)$ (yellow). The forcing Δ determines our initial starting point, and the recurrence follows the red or green trajectories. The final state $x_s(l \to \infty)$ is reached when the two functions, namely, $F(x)$ and $M_2(x)$, intersect. We observe three potential scenarios (Supplementary Section 2.5): Case 1 (**c**). $F(x)$ and $M_2(x)$ have a single intersection in $\mathfrak{B}_0$ (red). Under these conditions, regardless of Δ, the recurrence converges to $\mathbf{x}_s(l \to \infty) \in \mathfrak{B}_0$ and hence the system is structurally unrecoverable. Case 2 (**d**). $F(x)$ and $M_2(x)$ exhibit two intersections, corresponding to the system's two stable fixed points $\mathbf{x}_0$ (red) and $\mathbf{x}_1$ (green); the intermediate intersection (white dot) is unstable. Here for $\Delta < \Delta_c$, the system converges to $\mathfrak{B}_0$, that is, unrecoverable (red trajectory), whereas for $\Delta \geq \Delta_c$, it approaches $\mathfrak{B}_1$ and hence it is recoverable (green trajectory). Case 3 (**e**). If $F(x)$ is non-monotonic, the critical forcing Δ_c is determined by the local maximum point of $F(x)$ (Supplementary Section 2.5 provides a detailed analysis of Case 3). **f**, Structural recoverability is determined by the network topology (A, W) through κ, ω and ρ. A structurally unrecoverable (Case 1) system remains confined to $\mathfrak{B}_0$ and hence cannot be revived, even under arbitrarily large Δ. **g**, A structurally recoverable system (Cases 2 and 3) is unrecoverable if $\Delta < \Delta_c$ (left) and recoverable otherwise (right). Hence, the recoverable phase is driven by three structural parameters (κ, ω, ρ; grey) and a single dynamic parameter (Δ; orange).

retrieve the lost nodes, links or weights. To illustrate this difficulty, we refer to a concrete example below.

Example 1. Cellular dynamics (Fig. 3). As our first example, we consider the Michaelis–Menten model for gene regulation, capturing activation interactions between genes (Fig. 3a). Here $M_0(x_i) = -Bx_i^a$, an ath order depletion process[18], $M_1(x_i)=1$ and $M_2(x_j) = x_j^h/(1+x_j^h)$, a switch-like function that saturates to $M_2(x_j)\to 1$ for large x_j, representing the process of activation (Supplementary Section 3.1). The rate of this saturation is governed by h.

For sufficiently connected A or large average weight ω, the system exhibits an active state $\mathbf{x}_1$ in which all $x_{1,i}>0$—capturing a living cell. However, perturbations to A and W, such as link/node removal or weight loss can cause a sharp transition to the inactive state $\mathbf{x}_0=(0,\ldots,0)^\top$, describing cell death. To systematically track this transition, we measured the average activity $\bar{x}_\alpha = (1/N)\sum_{i=1}^N x_{\alpha,i}$, which follows $\bar{x}_\alpha > 0$ for $\alpha=1$ and $\bar{x}_\alpha = 0$ for $\alpha=0$. As we subject the system to increasing levels of stress, here reducing all the weights W by a factor $0\le q\le 1$, we observe a sudden transition at $q=q_c$ from $\mathbf{x}_1$ (Fig. 3b, green) to $\mathbf{x}_0$ (Fig. 3b, red). Next, we attempt to revive the node activities by retrieving the lost weights, finding that the system fails to recover. The reason is that although $\mathbf{x}_1$ is only stable for $q\le q_c$, $\mathbf{x}_0$ is always stable—both below and above this threshold. This leads to a hysteresis phenomenon, where the system remains inactive despite the reversal of perturbation.

Example 1, above—although representing a specific scenario—illustrates the family of challenges that we tackle here: system's with irreversible transitions that are driven by perturbations to their weighted topology. To revive such systems, we must not only restructure their lost topology but also dynamically reignite them by exerting external control over their activities $x_i(t)$.

Recoverability

The most natural way to reignite the system is to drive all activities x_i towards an initial condition from which the system naturally recovers to the desired $\mathbf{x}_1$. Namely, we must steer the system into $\mathbf{x}_1$'s basin of attraction:

$$\mathfrak{B}_1 = \{\mathbf{x}(t=0) \;\;|\;\; \mathbf{x}(t\to\infty)=\mathbf{x}_1\}, \tag{2}$$

which comprises all the initial conditions $\mathbf{x}(t=0)$ from which equation (1) converges to $\mathbf{x}(t\to\infty)=\mathbf{x}_1$ (Fig. 1h). The problem is that such level of control over the dynamics of all the nodes is seldom attainable; hence, we seek to recover the system's functionality by driving only a microscopic fraction $f\to 0$ of forced nodes.

To achieve this, we consider the limit $f\sim 1/N$ where our reigniting is typically attempted through a single, randomly selected source node s, whose activity we force to follow $x_s(t)=\phi(t)$. In many practical applications, our ability to exert such control—even on a single node—is restrictive, limiting the potential forms of $\phi(t)$. Hence, below, we reignite equation (1) using an extremely simple input, namely, $\phi(t)=$ constant. Other practically accessible forms of $\phi(t)$ are further considered in Supplementary Section 4. As simple as it is, the constant forcing itself is also constrained, as our forcing capacity is often bounded by $\phi(t)\le\Delta$. Therefore, we seek the conditions where such restricted interventions—controlling just one node and with a forcing bounded by Δ—can push the remaining nodes into the desired $\mathfrak{B}_1$.

During our intervention, the remaining $N-1$ nodes continue to follow the natural system dynamics of equation (1), as they respond to the s forcing. In technical terms, the failed state of the system, $\mathbf{x}_0$, captures the initial condition of equation (1), and the forced node imposes a strict boundary condition at s. In a recoverable system, after some time, the activities will enter $\mathfrak{B}_1$, at which point we can cease our external control and allow the system to naturally transition to $\mathbf{x}_1$, following its internal dynamics. If, however, the system is non-recoverable, such single-node reigniting is insufficient and the system remains at $\mathfrak{B}_0$; once we lift our forcing, it relaxes back to $\mathbf{x}_0$, resulting in a failed reigniting.

To analytically track the system's response to our forcing at s, we divide the rest of the network into shells $K_s(l)=\{j|L_{sj}=l\}$, comprising all the nodes located at distance l from s (Fig. 2a). In this notation, $K_s(0)=\{s\}$, $K_s(1)$ is the group of s's nearest outgoing neighbours, $K_s(2)$ its next-nearest neighbours and so on. Then, starting with $x_s(t)=\Delta$, we track the average activity of nodes in $K_s(l)$ via

$$x_s(l,t) = \frac{1}{|K_s(l)|}\sum_{i\in K_s(l)} x_i(t), \tag{3}$$

where $|K_s(l)|$ represents the number of nodes in $K_s(l)$. The shells adjacent to the source (small l) will be forced to respond to s's activation Δ. However, the distant shells (at $l\to\infty$) may be unaffected and therefore still remain within $\mathfrak{B}_0$. Under these conditions, upon the termination of our Δ forcing, all the shells retreat back to $\mathbf{x}_0$, rendering the system unrecoverable. Successful reigniting, therefore, requires that

$$x_s(l\to\infty, t\to\infty)\in\mathfrak{B}_1, \tag{4}$$

capturing a state in which the forcing at s can penetrate the network and affect the activity of even the most distant nodes at $K_s(l\to\infty)$. This represents a recoverable system that will naturally revert to $\mathbf{x}_1$ once our forcing Δ is deactivated. Note that in equation (4), we use the $\in$ sign loosely, as strictly speaking, $\mathfrak{B}_1$ includes the initial conditions of the form $\mathbf{x}$ and not scalar averages such as $x_s(l,t)$. Hence, equation (4) should be taken to imply the shell average $x_s(l\to\infty,t\to\infty)$ is congruent with a state $\mathbf{x}\in\mathfrak{B}_1$.

To obtain the final shell states $x_s(l)=x_s(l,t\to\infty)$, we use the fact that despite its potentially broad degree/weight distribution, our network is otherwise wired and assigned link weights at random (Supplementary Section 1). Therefore, (1) A features little degree correlations and hence the nodes in $K_s(l)$ are statistically similar to those in $K_s(l')$ (for $l,l'\ge 1$); (2) A is locally tree like, and therefore, asymptotically, there are almost no short-range loops surrounding the source s. Below, we relax both approximations when numerically testing our method against empirically constructed networks, which indeed feature both loops and measurable degree correlations (Supplementary Section 5.5). However, to advance analytically, we use approximations (1) and (2) above to translate equation (1) into a direct set of equations for $x_s(l)$. We arrive at the recurrence relation (Supplementary Section 2)

$$\begin{cases} x_s(0)=\Delta, \\ F(x_s(l)) = M_2\left(x_s(l-1)\right), \end{cases} \tag{5}$$

where

$$\begin{aligned} F(x) = {} & \tfrac{1}{\omega}R(x) - \rho\kappa M_2\left(R^{-1}\left(\omega M_2(x)+\omega\kappa M_2(\bar{\mathbf{x}}_0)\right)\right) \\ & -(1-\rho)\kappa M_2\left(\bar{\mathbf{x}}_0\right), \end{aligned} \tag{6}$$

in which $R(x)=-M_0(x)/M_1(x)$ and $R^{-1}(x)$ is its inverse function. In equation (6), parameter $\bar{\mathbf{x}}_0$ represents the mean activity of nodes in $K_s(l>1)$ under the failed state $\mathbf{x}_0$ (Supplementary Section 2.4). The remaining parameters are directly extracted from the weighted topology (A,W) as follows: ω is the average weight

$$\kappa = \frac{1}{N}\sum_{i=1}^N \frac{1}{|K_i(1)|}\sum_{j=1}^N A_{ij}^\top k_{j,\mathrm{in}} - 1 \tag{7}$$

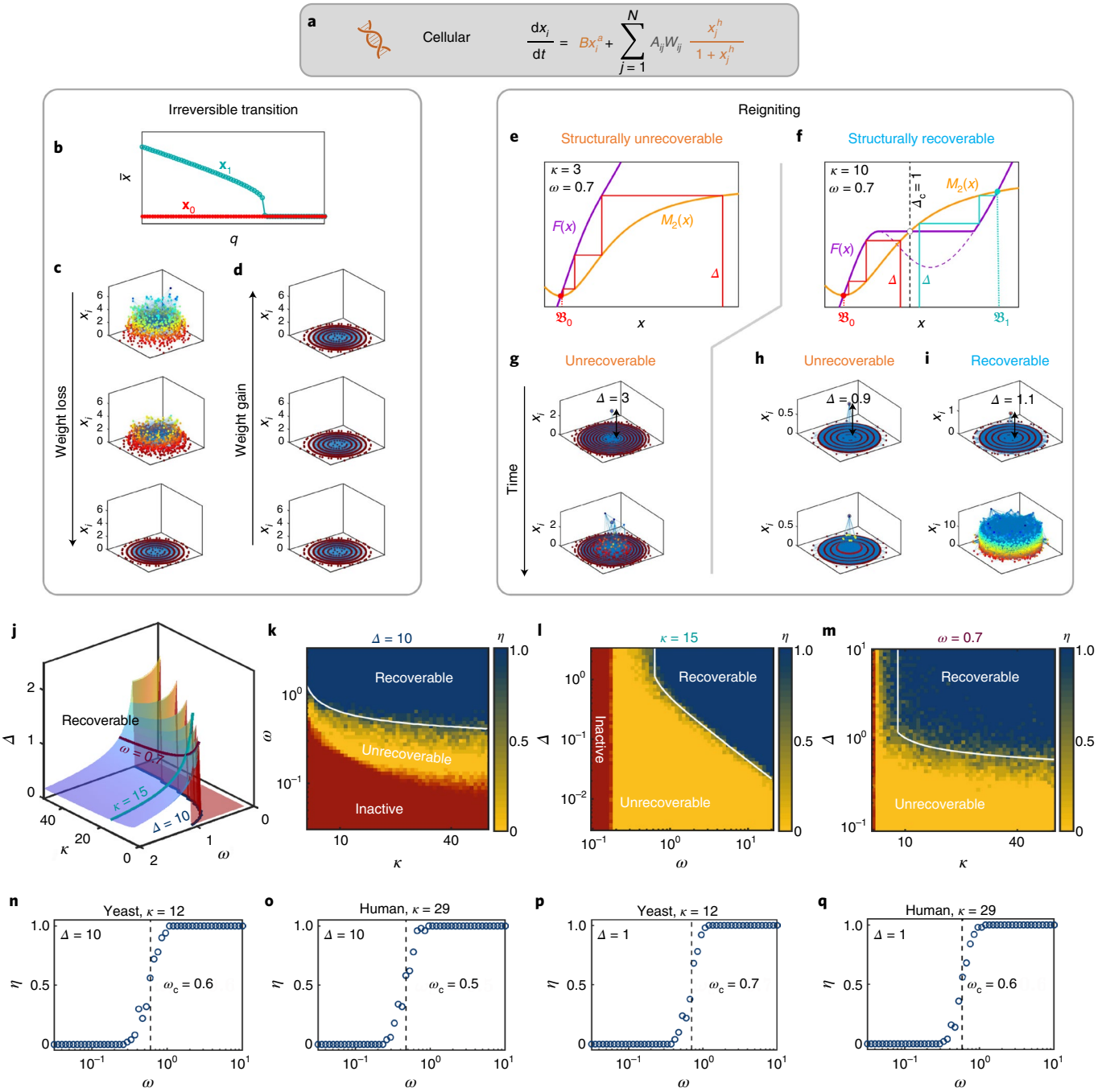

Fig. 3 | Recoverability of cellular dynamics. a, Michaelis–Menten model for subcellular dynamics. **b**, Average activity $\bar{x}$ versus weight reduction q ($q=0$: no reduction). Here $\mathbf{x}_1$ is only stable for $q \le q_c$ (green); $\mathbf{x}_0$ is always stable (red). **c**, We track x_i for three specific values of q. For small q (top), all $x_i > 0$, an active state $\mathbf{x}_1$. As q increases (weight loss), x_i become smaller (centre), until the system collapses into the inactive $\mathbf{x}_0$ (bottom). **d**, Retrieving the lost weights does not revive the system since $\mathbf{x}_0$ is always stable. Therefore, we must dynamically reignite the failed system. **e**, $F(x)$ (purple) and $M_2(x)$ (yellow) as obtained from the left-/right-hand sides of equation (9) with $\kappa=3$, $\omega=0.7$ and $\rho=1$. We observe Case 1 (Fig. 2c) with a single intersection at $\mathfrak{B}_0$ (red). This describes a structurally unrecoverable system. **f**, Under a denser A ($\kappa=10$), $F(x)$ changes form and the system now follows Case 3 in Fig. 2e (structurally recoverable) with $\Delta_c=1$ (vertical dashed line). **g**, Forcing s (black node) to a permanent Δ activity, no matter how large, fails to reignite the structurally unrecoverable system of **e**. **h**,**i**, Reigniting fails for $\Delta=0.9$ (**h**), but succeeds for $\Delta=1.1$ (**i**), confirming our predicted $\Delta_c=1$ in **f**. **j**, The phase diagram in the (κ, ω, Δ) space. The red area in (κ, ω) captures the structurally unrecoverable regime. We show three specific cross-sections, fixing Δ (blue), κ (green) and ω (red), to be expanded in **k**–**m**. **k**, The (κ, ω) phase diagram, as obtained from 5×10^4 scale-free networks (Supplementary Section 5.3). Each data point represents the fraction η of successful reigniting instances across 20 independent attempts. We observe the predicted phases: inactive (red), where only $\mathbf{x}_0$ is stable; unrecoverable ($\eta=0$; yellow); and recoverable ($\eta=1$; blue), where single-node reigniting is possible. Our theoretical prediction is also shown (white solid line). **l**,**m**, The (ω, Δ) (**l**) and (κ, Δ) (**m**) phase diagrams. For $\omega<0.6$ (**l**) and $\kappa<8$ (**m**), the system is structurally unrecoverable and hence $\Delta_c \to \infty$. The theoretical prediction is also shown (white solid lines). **n**,**o**, η versus ω as obtained from yeast (**n**) and human (**o**) protein interaction networks ($\kappa=12$ and 29; $\Delta=10$). For $\omega<\omega_c$ (vertical dashed lines), reigniting fails ($\eta=0$); above it, reigniting is successful ($\eta=1$), as predicted. **p**,**q**, Similar results for yeast (**p**) and human (**q**) networks under $\Delta=1$.

represents the average neighbour's residual in degree[13,23], and $\rho = P(A_{ij} = 1|A_{ij}^{\top} = 1)$ describes the network's reciprocity, capturing the probability to observe a link $i \to j$ given the existence of $j \to i$ (for undirected networks, $\rho = 1$).

Equations (5) and (6) represent our key result. They approximate the recoverability of equation (1), a multidimensional nonlinear dynamic equation, through a manageable first-order recurrence relation. This recurrence takes the system's weighted topology (κ, ρ and ω) and its nonlinear dynamics (M_0, M_1 and M_2) as the input, and, together with our intervention constraints (Δ), predicts the system's recoverability as the output. Indeed, for any given forcing Δ, the recurrence in equation (5) either converges to $x_s(l \to \infty) \in \mathfrak{B}_1$, satisfying the recoverability condition in equation (4), or to $x_s(l \to \infty) \in \mathfrak{B}_0$, indicating a failed recovery.

To obtain $x_s(l \to \infty)$, we extract the stationary states of equation (5), requiring[24,25]

$$F(x) = M_2(x), \tag{8}$$

which, in turn, provides $x_s(l) = x_s(l-1)$. Depending on κ, ω and ρ, we observe two characteristic behaviours (Fig. 2 and Supplementary Section 2.5). Structurally unrecoverable (Fig. 2c,f): if $F(x)$ and $M_2(x)$ have a single intersection $x \in \mathfrak{B}_0$, then the series in equation (5) inevitably converges to that point. This captures structural unrecoverability, where regardless of Δ, single-node reigniting is prohibited. Structurally recoverable (Fig. 2d,e,g): if, on the other hand, $F(x)$ and $M_2(x)$ have several intersections, then the convergence of equation (5) depends on the boundary condition $x_s(0) = \Delta$, whose magnitude is determined by our forcing capacity. For $\Delta < \Delta_c$, our forcing is too small, and the system approaches $\mathfrak{B}_0$, a failed reigniting. For $\Delta \geq \Delta_c$, it will reach $\mathfrak{B}_1$, capturing a successful reigniting. In case a system is structurally recoverable and $\Delta \geq \Delta_c$, we say that it is in the recoverable phase—a state in which one can revive the system by forcing only one node (Fig. 2i).

Taken together, for a given dynamics $M_0(x)$, $M_1(x)$ and $M_2(x)$, our formalism predicts a four-dimensional phase diagram in the phase space of κ, ρ, ω and Δ, defining the boundaries of recoverability. Next, we investigate this phase space on a range of relevant systems, from cellular dynamics (Example 1) to neuronal and microbial systems. In our first example below, we consider, for simplicity, undirected networks ($\rho = 1$), reducing our phase space to three relevant dimensions, namely, κ, ω and Δ. Our final example (reviving a dysfunctional microbiome) examines recoverability under directed interactions ($\rho < 1$).

Applications

Example 1 cellular dynamics. As our first application (Fig. 3 and Supplementary Section 3.1), we return to Example 1, regulatory dynamics, where $M_0(x) = -x^a$, $M_1(x) = 1$ and $M_2(x) = x^h/(1+x^h)$ and therefore $R(x) = x^a$ and $R^{-1}(x) = x^{1/a}$. Equation (8) under $\rho = 1$ becomes

$$\frac{1}{\omega}x^a - \frac{\kappa x^{\frac{h^2}{a}}}{x^{\frac{h^2}{a}} + \omega^{-\frac{h}{a}}(1+x^h)^{\frac{h}{a}}} = \frac{x^h}{1+x^h}, \tag{9}$$

whose roots (x) determine the potential fixed points of the reignited system. Clearly, $x = 0$ is a solution, capturing the fact that the failed state $\mathbf{x}_0 = (0, \ldots, 0)^{\top} \in \mathfrak{B}_0$ is always stable. Hence, the question is under what conditions do we observe a second solution $x > 0$, representing a potential convergence to $\mathfrak{B}_1$. To answer this, in Fig. 3e,f, we plot $M_2(x)$ versus x (yellow) and observe its intersections with $F(x)$ (purple) as we vary the values of κ and ω. This allows us to graphically observe the potential convergence of the system to $\mathfrak{B}_0$ or $\mathfrak{B}_1$.

First, we consider $\kappa = 3$ and $\omega = 0.7$ (Fig. 3e). We find that equation (9) exhibits only one solution, represented by the single intersection at $x = 0$ (red dot). This guarantees that equation (5) converges to $x_s(l \to \infty) = 0$, independently of Δ. Consequently, the system is structurally unrecoverable. Indeed, Fig. 3g indicates that despite the forcing Δ at s, the system fails to reactivate.

Increasing the network density to $\kappa = 10$, however, changes the picture; now, equation (9) features three intersection points (Fig. 3f): an intermediate unstable point (white) and two stable points at $x = 0$ (red) and $x > 0$ (green), representing convergence to $\mathfrak{B}_0$ and $\mathfrak{B}_1$, respectively. Hence, the system is now structurally recoverable, with critical forcing $\Delta_c = 1$ (vertical dashed line), above which it enters the recoverable phase. This prediction is corroborated in Fig. 3h,i: under $\Delta = 0.9$, the system remains in $\mathfrak{B}_0$, but for $\Delta = 1.1$, just above Δ_c, it successfully reignites, as precisely predicted.

This uncovers the existence of a previously overlooked dynamic phase of the Michaelis–Menten model. Indeed, the regulatory system shown in Fig. 3a has been previously[13] shown to follow two phases: inactive (where only $\mathbf{x}_0$ is stable) and bistable (where both $\mathbf{x}_0$ and $\mathbf{x}_1$ are stable) (Fig. 3b–d). Yet, we now unveil a third phase, recoverable, a subspace of the bistable phase in which the system can be reignited from $\mathbf{x}_0$ to $\mathbf{x}_1$ by controlling a single node.

To systematically examine this phase space, we present the recoverability phase diagram (Fig. 3j). For small κ and ω, we observe the structurally unrecoverable regime in which recoverability is unattainable even with arbitrarily large Δ (red patch in the κ–ω plane). The remaining area in (κ, ω) represents the structurally recoverable regime, which is split between the unrecoverable phase (for $\Delta < \Delta_c$ (below surface)) and the recoverable phase when $\Delta \geq \Delta_c$ (above surface).

Setting Δ as constant, in Fig. 3k, we construct the (ω, κ) phase diagram by numerically simulating the regulatory dynamics on an ensemble of 5×10^4 scale-free networks, covering 2,500 distinct combinations of ω and κ (Supplementary Section 5.3). Each data point in Fig. 3k captures the fraction of successful recoveries η among 20 independent reigniting trials, from zero successes ($\eta = 0$; yellow) to 100% successful recovery attempts ($\eta = 1$; blue); the white solid line represents our theoretical

Fig. 4 | Two-step recovery for reviving a failed cellular system. a, Unperturbed yeast protein interaction network. For visibility, we focus on the circled subnetwork. **b**, As expected, the unperturbed network is in the active state $\mathbf{x}_1$; hence, all $x_i > 0$. **c**,**d**, After extensive perturbation in which 30% of nodes/links (grey and red) were deleted, the state of the network collapses to the inactive $\mathbf{x}_0$, in which all $x_i = 0$. The challenge is that some of the deleted components (nodes/links) are inaccessible and hence cannot be retrieved (red). This captures restructuring constraints that are, indeed, inevitable in realistic scenarios. The circle at the centre: we focus on the same subnetwork shown in **a**, the deleted nodes/links appear in grey and red, and the remaining unperturbed components are highlighted. **e**, Step I. Within the given constraints, we restructure the network by reintroducing nodes/links or strengthening link weights. We map these interventions into their impact on the two relevant control parameters, namely, κ (blue) and ω (orange). For illustration, we show the highlighted subnetwork of **c** as it restructures, acquiring nodes, links and increased weights (subnetworks along the x axis). **f**, Restructuring paths in the phase diagram of (κ, ω). A successful path leads the network from the collapsed phase (red) into the recoverable phase (blue). Using our predicted phase boundary (white solid line), we design several alternative paths, affording us flexibility to, for example, focus on increasing weights ω (Net 1; light-blue path) or enhancing network density κ (Net 3; purple path); as dictated by the nature of our constraints. **g**, Step II. Once the network is in the recoverable phase, we can revive it via single-node reigniting, demonstrated here on each of our restructured networks, namely, Nets 1–3.

prediction based on analysing the intersections of equation (9). We find that the boundaries of recoverability (Fig. 3k–m, yellow/blue regions) can be well approximated by our analytical framework. We also present the phase diagram in the (ω,Δ) and (κ,Δ) spaces (Fig. 3l,m, respectively), further confirming our predicted transitions.

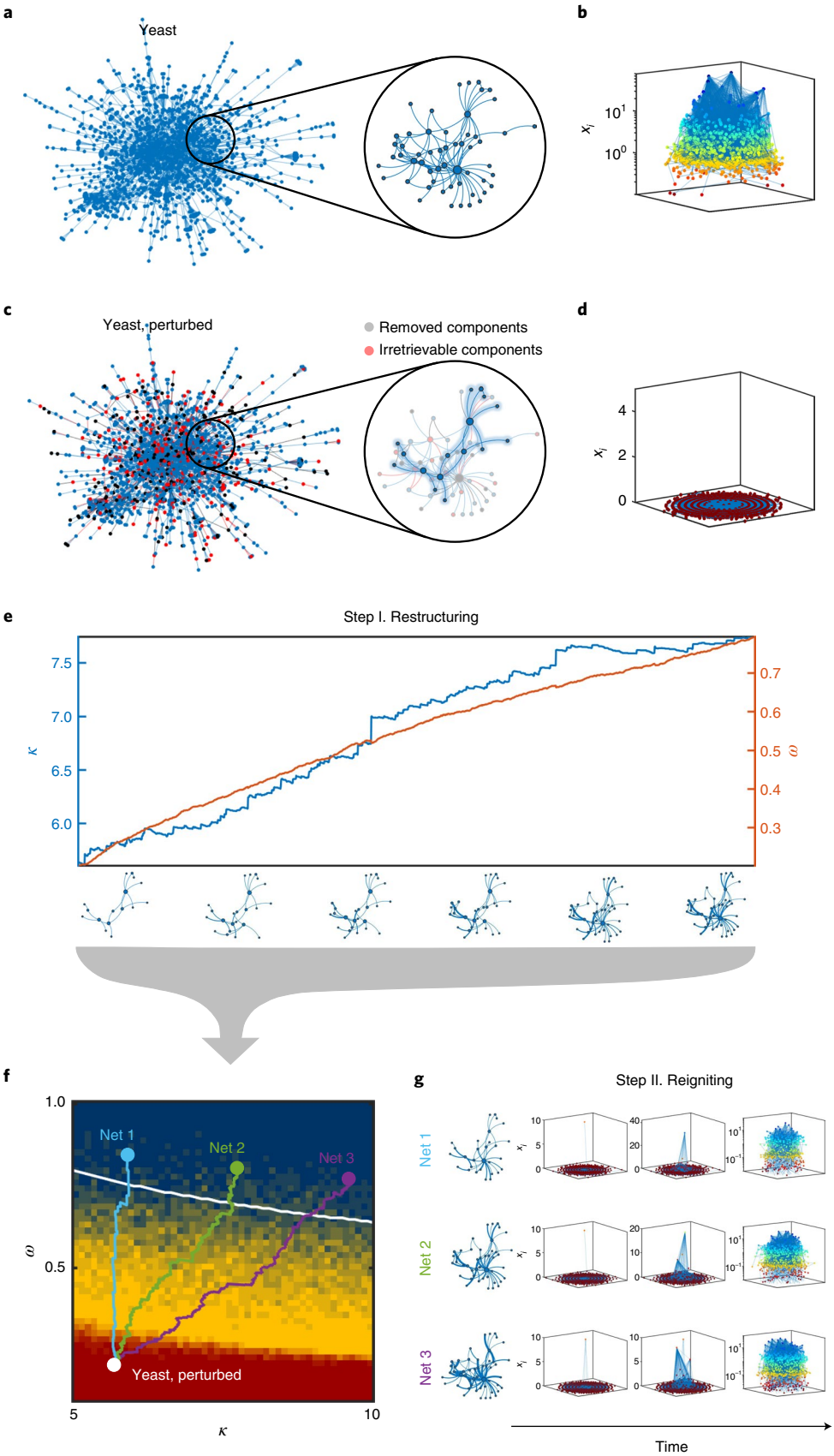

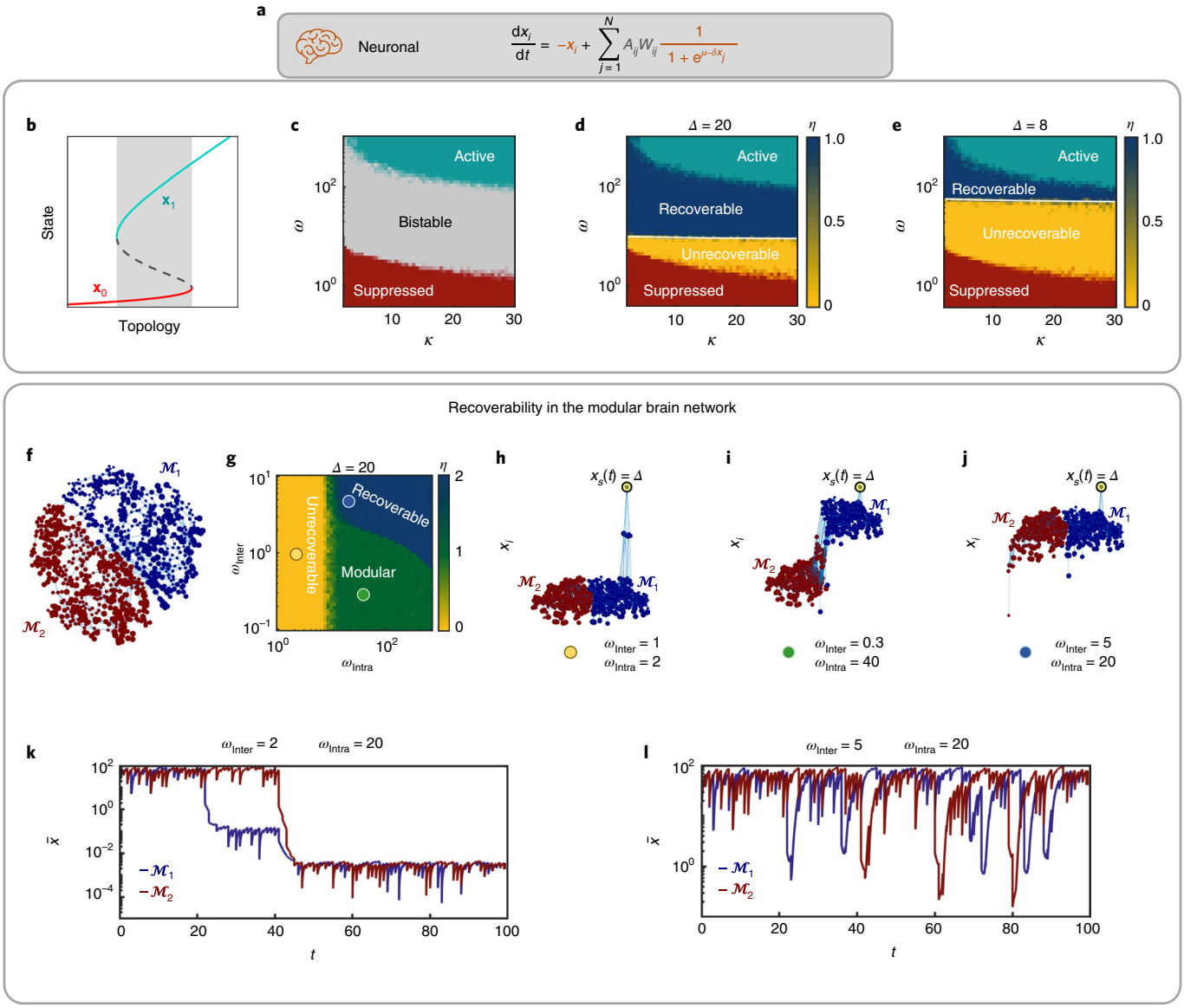

Fig. 5 | Recoverability of neuronal dynamics. a, Wilson–Cowan neuronal dynamics (we use a modified version of the model that can be cast in the form of equation (1); Supplementary Section 3.2). **b**, The system exhibits three states: suppressed $\mathbf{x}_0$ (red) when κ and ω are small; active $\mathbf{x}_1$ (green) under large κ and ω; bistable (centre; shaded grey) in which both $\mathbf{x}_0$ and $\mathbf{x}_1$ are stable. **c**, The three states, namely, suppressed (red), active (green) and bistable (grey), as obtained from 5×10^4 scale-free networks capturing distinct combinations of κ and ω. **d**,**e**, The recoverability phase diagram in the (κ,ω) space under $\Delta=20$ (**d**) and $\Delta=8$ (**e**). Each data point represents 20 independent realizations. As predicted, the bistable state is split into two distinct dynamic phases—unrecoverable (yellow) and recoverable (blue). The simulation results (yellow–blue transition) are in perfect agreement with our theoretical predictions (white solid lines). **f**, Empirically constructed brain network and its two hemispheres $\mathcal{M}_1$ (blue) and $\mathcal{M}_2$ (red). **g**, We measured the reigniting success rate η of the modular brain network along the phase diagram of $(\omega_{Intra}, \omega_{Inter})$ (Methods). We observe three phases: unrecoverable in which no module can be revived ($\eta=0$; yellow); recoverable in which both modules reactivate ($\eta=2$; blue); and modular in which reigniting is constrained to a single module ($\eta=1$; green). **h**, Setting $\omega_{Inter}=1$ and $\omega_{Intra}=2$ in the unrecoverable phase (yellow circle), we indeed find that reigniting fails to revive both of the modules. **i**, In the modular phase (green circle), $\mathcal{M}_1$ recovers, but fails to reactivate $\mathcal{M}_2$. **j**, In the recoverable phase (blue circle), reigniting successfully crosses over from $\mathcal{M}_1$ to $\mathcal{M}_2$. **k**, The average activity $\bar{\mathbf{x}}$ of $\mathcal{M}_1$ (blue) and $\mathcal{M}_2$ (red) versus t, as obtained from numerically simulating neuronal dynamics on the brain network. Adding noise, we observe sporadic fluctuations, some causing a transition to the suppressed state. The first collapse occurs to $\mathcal{M}_1$ at $t\approx20$. Soon after, $\mathcal{M}_2$ also collapses at $t\approx40$, and the entire network irreversibly fails. **l**, Increasing the intermodule weights to $\omega_{Inter}=5$, we enter the recoverable phase. Now, when one module fails, the other module reignites it. This captures a fail-safe system whose modular structure provides internally embedded self-recoverability.

To test our predictions in an empirical setting, we collected data on two real biological networks, capturing protein interactions in human[26] ($\kappa=29$) and yeast[27] ($\kappa=12$) cells. Varying ω and Δ, we measured the reigniting success rate η. In both networks, we observe a sharp transition into the recoverable phase (Fig. 3n–q), which precisely falls on the theoretically predicted phase boundary (ω_c; vertical dashed lines).

Restructuring guidelines. In case our system is not in the recoverable phase, we must design appropriate restructuring interventions

to push ω or κ towards recoverability (Fig. 4). In a cellular environment, this can be achieved through biochemical interventions that help catalyse or inhibit specific reactions[28]. The phase diagrams shown in Fig. 3j–m, which map the boundaries of the recoverable phase, can help us design such interventions.

To illustrate this, in Fig. 4a–d, we simulate a cellular network (yeast) that has been driven towards inactivity due to a series of node/link deletion (grey nodes/links). Some of the removed components are inaccessible (red) and hence cannot be retrieved during restructuring. With these constraints in mind, we incorporate our two-step strategy: Step I. Restructuring. We design a sequence of accessible interventions on (A, W) to bring the network closer to the recoverable phase. An example of such a sequence is shown in Fig. 4e (along the x axis). On the y axis, we present the accumulating impact of these restructuring interventions on κ (blue) and ω (orange). To revive the system, we seek paths of such accessible interventions that help deliver the network into the bounds of the recoverable phase (Fig. 4f). Our goal, we emphasize, is not to simply retrieve the lost components but to achieve recoverability. This designates not a single point but rather an entire subspace in (κ, ω) (Fig. 4f, blue area), affording us some level of restructuring flexibility. Indeed, despite the network's irretrievable components, we were able to design three distinct restructuring paths, leading to different destinations—namely, Nets 1, 2 and 3—all within the recoverable subspace (Fig. 4f, blue area). Step II. Reigniting. Once in the recoverable phase, we can revive the system via single-node reigniting as shown in Fig. 4g for Nets 1, 2 and 3.

This example illustrates how the phase diagrams of recoverability provide guidelines for restructuring. For example, in Fig. 4f, path 1 mainly builds on controlling the interaction strengths (ω), but assumes little freedom to add nodes or links (κ). In contrast, path 3 involves a significant component of adding nodes/links to A, affecting not only ω but also κ. The optimal restructuring path is, therefore, determined by the nature of our constraints, for example, the relative difficulty in adding weights versus adding nodes/links. Although the potential space of structural interventions in Step I is incomprehensibly vast, our phase diagrams reduce this space into only two relevant control parameters, κ and ω (and ρ if A is directed). This reduction allows us to assess the contribution of all potential interventions by quantifying their effect on these two (or three) parameters—providing optimal pathways towards recoverability (Supplementary Section 3.1.3).

Example 2 neuronal dynamics. As our second example (Fig. 5 and Supplementary Section 3.2), we consider the Wilson–Cowan neuronal dynamics[29,30,31] in which equation (1) follows the form shown in Fig. 5a (we use a modified version of the model that can be cast in the form of equation (1); Supplementary Section 3.2.) The system naturally exhibits two dynamic states (Fig. 5b): suppressed ($\mathbf{x}_0$, red) in which all the activities are constricted; active ($\mathbf{x}_1$, green) where x_i are relatively large (green). In between these two extremes lies a bistable phase in which both $\mathbf{x}_0$ and $\mathbf{x}_1$ are potentially stable (shaded grey). This predicts a hysteresis phenomenon in which a system driven to the left of the grey area will avoid spontaneous recovery.

To observe the predicted phases, in Fig. 5c, we numerically analyse our ensemble of 5×10^4 scale-free networks. We indeed find the active (green) and suppressed (red) phases, separated by the strip of bistability (grey). Our formalism, however, predicts an additional dynamic phase, recoverable. This phase (Fig. 5d,e, blue area) identifies a subspace within the bistable regime, under which the system can be driven to $\mathbf{x}_1$ via single-node reigniting; the theoretically predicted phase boundaries are also shown (white solid lines), precisely capturing the numerically observed transitions (yellow/blue area).

In Methods, we further demonstrate how the brain's modular structure impacts the recoverability phase space. We also characterize conditions under which modularity provides a fail-safe mechanism in which one module revives the other upon failure.

Example 3 microbial dynamics. As our final example (Fig. 6 and Supplementary Section 3.3), we consider the gut microbiome, a microbial community whose functional state has been shown to crucially impact human health[32,33]. Following perturbations such as antibiotic treatment, the abundance of different species may reach critical levels, potentially leading to a dysfunctional microbiome[34]. We, therefore, examine below how our two-step revival strategy can help steer a failed microbiome back to functionality.

To construct the interaction network, we collected data[35] describing the metabolic in/out flux of $N=838$ microbial species, allowing us to map their complementary chemical interactions. A cooperative link $i\rightarrow j$ appears when species i produces a resource consumed by j (ref. [36]); an adversarial link $i\leftrightarrow j$ is assigned if both i and j compete over the same resource[37]. The weight W_{ij} of each link captures the level of interspecies reliance: for example, if i is the sole producer of j's only consumed nutrient m, then j's growth strongly depends on i. If, however, there are many alternative producers of m or if m is only one of j's many consumed nutrients, then W_{ij} will be small. We arrive at a directed and highly diverse network with broadly distributed weights, and most crucially, with ~75% adversarial interactions, in which $W_{ij}<0$ (Fig. 6b,c and Supplementary Section 3.3.3). This challenges our theoretical framework, which is primarily designed around cooperative interactions, and therefore helps us test its applicability limits.

To track the microbial populations, we used the dynamics shown in Fig. 6a. The self-dynamics combines logistic growth with the Allee effect[38], and the interspecies cooperative/adversarial interactions follow the Lotka–Volterra dynamics[22]. The parameter F captures the externally introduced microbial influx. Out of the original pool of N species, we find that 32% cannot be supported by the network and undergo extinction. The remaining 568 species, comprising the actual microbiome composition, exhibit two potential fixed

Fig. 6 | Recoverability of microbial dynamics. a, Population dynamics. **b**, Export (orange)–import (green) network, linking microbial species to the nutrients they produce/consume. Cooperative links (blue) are assigned when i's exports are imported by j; adversarial links (red) are assigned when i and j share mutual import(s). **c**, The resulting gut microbiome, a diverse weighted and directed network with mixed cooperative (blue) and adversarial (red) links. **d**–**f**, The system exhibits two states (**d**): functional $\mathbf{x}_1$ (**e**, green diamond) or dysfunctional $\mathbf{x}_0$ (**f**, red diamond), with a broad range of bistability (shaded grey). **g**, Propagation of a reigniting signal: $s\rightarrow i\rightarrow j$. In Methods, we show that an effective $i\rightarrow j$ link must satisfy $W_{i\rightarrow j}>w_0$. **h**, Counting only effective links, we obtain the reigniting capacity of s ($\mathcal{R}_s$) as the number of potentially reactivated nodes (blue). **i**, We ranked all the microbial species based on $\mathcal{R}_s$, identifying the network's most effective reigniters. The top 26 nodes stand out, with $\mathcal{R}_s$ that is orders of magnitude higher than the rest. **j**, Visibly dense effective network surrounding *B. bifidum* ($\mathcal{R}_s=360$). As expected, *B. bifidum* successfully reignites the microbiome (right). **k**,**l**, We examined two lower-ranked species (*P. putida* (**k**) and *P. distasonis* (**l**)) that failed to revive the network. Specifically, *P. putida*—despite having a high $\mathcal{R}_s$—only causes a local impact but fails to revive the network. **m**, To reignite with *P. putida*, we employ our two-step strategy. In Step I, we use nutritional supplements (green) to eliminate competitive links (red dashed link) by ensuring nutrient availability. **n**, We ranked nutrients based on their contribution to the adversarial links. The top three nutrients by rank are highlighted (green). **o**, Supplementing these three nutrients via dietary interventions, we restructure the microbial network, reducing adversarial interactions (red). The insets allow a visible comparison, showing the removed adversarial links (red). **p**, In Step II, we administer probiotics to boost the population of a specific species. **q**, After restructuring, we find that *P. putida*, an originally failed reigniter, can now successfully revive the microbiome.

points (Fig. 6d–f), functional $\mathbf{x}_1$ and dysfunctional $\mathbf{x}_0$. Our goal is to apply our two-step recoverability strategy to drive a dysfunctional microbiome at $\mathbf{x}_0$ back towards $\mathbf{x}_1$.

Selective reigniting. In Methods, we show how to evaluate each node's reigniting capacity $\mathcal{R}_s$, allowing us to rank all the candidate reigniter species in the microbiome, based on their potential

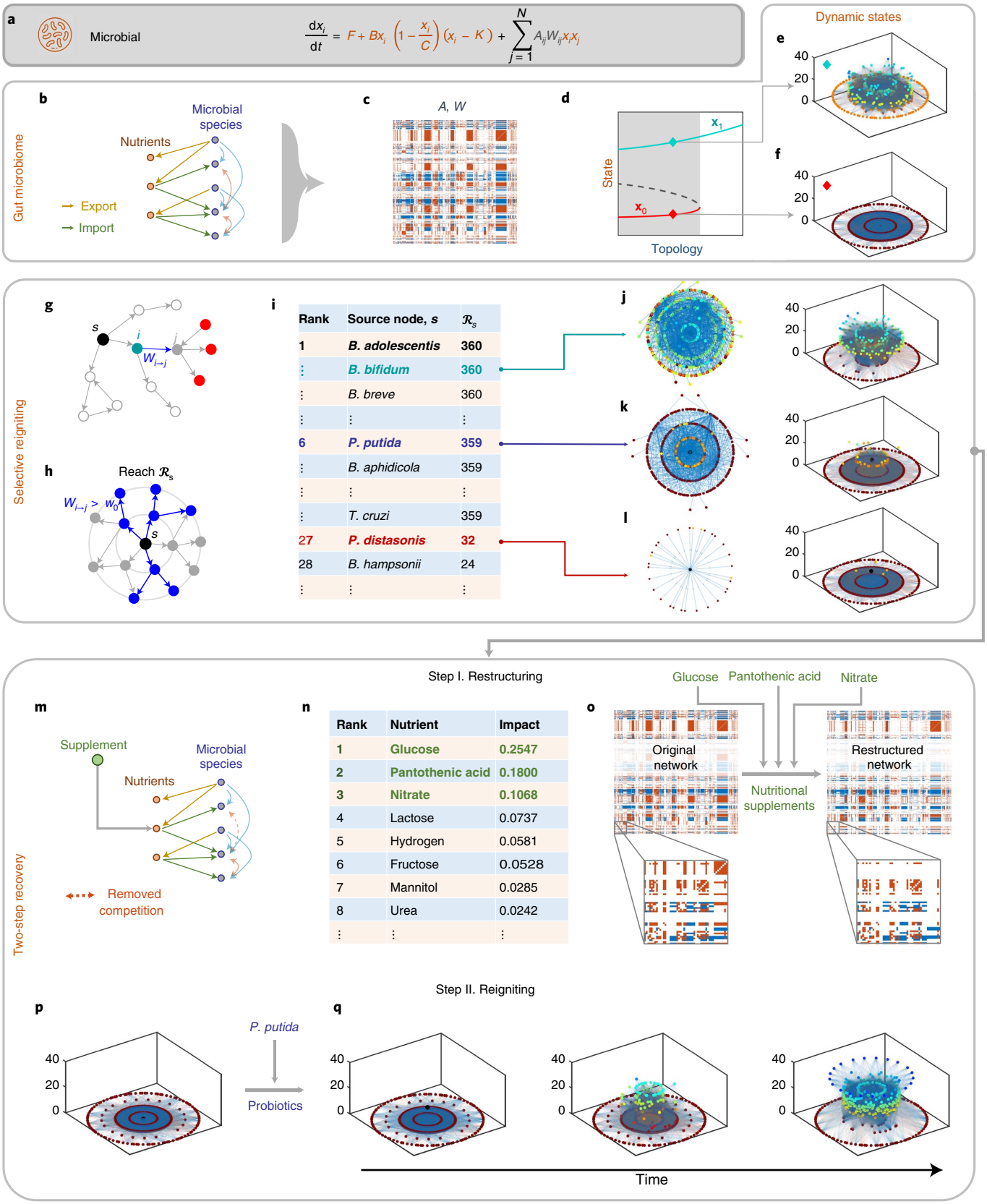

to revive the system (Fig. 6g,h). For a random topology, where all the shells $K_s(l)$ are statistically similar, we expect minor differences in $\mathcal{R}_s$ between the nodes. Here, however, we find that $\mathcal{R}_s$ is highly diverse, with the top 26 species having $\mathcal{R}_s > 300$, and the remaining species with $\mathcal{R}_s$ that is one or two orders of magnitude lower (Fig. 6i). Such diversity—a consequence of the unique non-random structure of the microbiome—indicates that in this system, the top 26 nodes represent preferred candidates for reigniting. To examine this, we attempted to sequentially reignite the microbiome with each of the nodes, finding that, indeed, success was by far more likely among the top-ranked reigniters (Fig. 6j–l and Methods).

One exception that we identified among these top reigniters is *P. putida*, which despite having $\mathcal{R}_s = 359$ and ranking sixth in the reigniters list, still falls short of reviving the system (Fig. 6k). This is due to the fact that *P. putida*'s reigniting capacity is hindered by its many surrounding adversarial interactions. Indeed, reigniting—by its nature—builds on the positive activation that the source species s exerts on its neighbours at $K_s(l)$. Such a positive impact is undermined by negative links. Next, we use *P. putida*'s restricted reigniting capacity as an opportunity to examine our two-step strategy in a realistic setting.

Two-step recovery of a dysfunctional microbiome. Consider a microbial network at state $\mathbf{x}_0$ that we wish to recover. Among the many practical constraints on our potential interventions, one crucial constraint is that we lack control over the majority of microbial species and hence we must achieve recovery with a handful of accessible reigniting nodes. Specifically, let us assume that our top accessible candidate for reigniting is precisely *P. putida*, which cannot revive the system by itself (Fig. 6k). Hence, we employ our two-step strategy. Step I. Restructuring. To enhance *P. putida*'s reigniting capacity, we wish to inhibit the adversarial interactions, which stand in the way of the system's reactivation. We consider two potential interventions. (1) Removing selected nodes that have many adversarial interactions (competition hubs) by means of targeted narrow-spectrum antibiotic treatment. (2) Deleting or weakening adversarial links through nutritional or biological interventions[39,40]. For example, if i and j compete over metabolite m, we prescribe dietary supplements to ensure the availability of m, thus eliminating the (i,j) competitive interaction (Fig. 6m). Since antibiotic intervention on an already dysfunctional microbiome may cause additional risks, here we implement restructuring via intervention (2) above. First, we rank all the nutrients based on their relative contribution to the adversarial weights in W (Fig. 6n and Supplementary Section 3.3.3). We then supplement the top three nutrients in the list (green) to restructure the network. Eliminating the competition over these now freely available nutrients, we arrive at our restructured network, which—owing to our interventions—now has a more suitable balance of cooperative versus adversarial interactions (Fig. 6o). Step II. Reigniting. In the microbiome, forcing can be implemented by administering probiotics, a common therapeutic practice that helps artificially sustain a desired abundance of a selected species[41]. The rate of probiotic intake determines the average activation force, set to be above the reigniting threshold Δ_c. Having restructured the network, we now attempt, once again, to reignite it with *P. putida*. We find that the originally failed reigniter is now capable of reviving the inactive microbiome (Fig. 6p,q).

Applicability limits. Our theoretical analysis helps construct the precise phase diagrams in the (κ,ω,Δ) phase space, predicting the bounds of the recoverable phase. These analytically tractable observations rely on a specific set of assumptions, mainly that A features marginal degree correlations and has a scarcity of short-range loops and that the dynamics is of the form of equation (1) and has primarily cooperative interactions. A precise description of these modelling assumptions is provided in Supplementary Section 1.

Our applications, however, provide insights that extend well beyond these analytical limits. For example, all our empirical networks—cellular, neuronal and microbial—exhibit non-negligible deviations from the above assumptions; yet, our analysis correctly predicted their recoverability (Supplementary Section 5.5). The gut-microbiome analysis helped us derive implementable guidelines for reigniting, also including the notion of selective reigniting, despite the network's strong degree correlations and significant share of adversarial links (Fig. 6). In Supplementary Section 3.4, we further consider diffusive interactions in which the governing equation is generalized beyond the form of equation (1). We also analyse alternative forms of reigniting, using periodic activity boosts, which in certain applications may be more accessible than the time-independent forcing (Δ) considered here (Supplementary Section 4).

Discussion and outlook

While the structure of complex networks has been deeply investigated over the years, our understanding of their dynamics is still emerging. The challenge is often focused on prediction, aiming to foresee a network's dynamic behaviour. Here we go a step further and focus on influence, showing how to steer a system towards a desired behaviour.

Our solution seals a crucial gap in our pursuit of the controllability of a nonlinear system[42]. Existing approaches often rely on specific system symmetries[43–45], which do not cover complex systems of the form of equation (1). In the absence of such symmetries, complex system control is frequently studied by means of linearization[46,47], using linear approximation to help capture the system's local behaviour in the vicinity of each of its fixed point. Such local analysis, however, is insufficient in the context of recoverability, as here we seek to drive the system outside its current basin and consequently beyond the linear regime. To overcome this restriction of locality, cross-basin control was recently developed using time-varying inputs that adapt until the system is pushed—step by step—into the desired basin of attraction[14]. Although highly effective, such interventions require a detailed control over the nodes' dynamics, first monitoring the system's response and then updating—in real-time—the form of our intervention. Such level of observation/control is not always guaranteed.

To break this gridlock, we seek non-local control across basins, but with simple dynamic interventions that do not require highly detailed input signals. Our recoverability phase diagram addresses this by identifying unique conditions where such control is attainable. On the one hand, pushing the system between macroscopic states, but on the other hand, using an extremely crude and simple control input—a time-limited constant activation Δ that is applied to only one or few nodes. No fine-tuning or real-time update of the input signal is required. Indeed, all that is needed is a strong enough jolt to the system, after which it naturally relaxes to its desired target state.

The microscopic behaviour of complex networks is driven by countless parameters, from the fine structure of A and W to the specific rates of each node's dynamic processes. Our analysis, however, shows that their large-scale functionality can be traced to a manageable set of relevant parameters, namely, κ, ω, ρ and Δ. Such dimension reduction is the fundamental premise of statistical physics, allowing the analysis of systems with endless degrees of freedom using a limited set of statistical entries. We believe that such an approach to network dynamics can help us understand, predict and ultimately influence the behaviour of these complex multidimensional systems.

Online content

Any methods, additional references, Nature Research reporting summaries, source data, extended data, supplementary information, acknowledgements, peer review information; details of

author contributions and competing interests; and statements of data and code availability are available at https://doi.org/10.1038/s41567-021-01474-y.

Received: 25 November 2020; Accepted: 19 November 2021;
Published online: 20 January 2022

References

1. Van Mieghem, P. *Graph Spectra for Complex Networks* (Cambridge Univ. Press, 2010).
2. Zhao, J., Li, D., Sanhedrai, H., Cohen, R. & Havlin, S. Spatio-temporal propagation of cascading overload failures in spatially embedded networks. *Nat. Commun.* **7**, 10094 (2016).
3. Dobson, I., Carreras, B. A., Lynch, V. E. & Newman, D. E. Complex systems analysis of series of blackouts: cascading failure, critical points, and self-organization. *Chaos* **17**, 026103 (2007).
4. Shih, H.-Y., Hsieh, T.-L. & Goldenfeld, N. Ecological collapse and the emergence of travelling waves at the onset of shear turbulence. *Nat. Phys.* **12**, 245–248 (2016).
5. Jiang, J., Hastings, A. & Lai, Y.-C. Harnessing tipping points in complex ecological networks. *J. R. Soc. Interface* **16**, 20190345 (2019).
6. May, R. M. Thresholds and breakpoints in ecosystems with a multiplicity of stable states. *Nature* **269**, 471–477 (1977).
7. Cohen, R., Erez, K., Ben-Avraham, D. & Havlin, S. Breakdown of the Internet under intentional attack. *Phys. Rev. Lett.* **86**, 3682 (2001).
8. Schreier, H. I., Soen, Y. & Brenner, N. Exploratory adaptation in large random networks. *Nat. Commun.* **8**, 14826 (2017).
9. Motter, A. E. & Lai, Y.-C. Cascade-based attacks on complex networks. *Phys. Rev. E* **66**, 065102 (2002).
10. Crucitti, P., Latora, V. & Marchiori, M. Model for cascading failures in complex networks. *Phys. Rev. E* **69**, 045104 (2004).
11. Achlioptas, D., D'Souza, R. M. & Spencer, J. Explosive percolation in random networks. *Science* **323**, 1453–1455 (2009).
12. Boccaletti, S. et al. Explosive transitions in complex networks structure and dynamics: percolation and synchronization. *Phys. Rep.* **660**, 1–94 (2016).
13. Gao, J., Barzel, B. & Barabási, A.-L. Universal resilience patterns in complex networks. *Nature* **530**, 307–312 (2016).
14. Cornelius, S. P., Kath, W. L. & Motter, A. E. Realistic control of network dynamics. *Nat. Commun.* **4**, 1942 (2013).
15. Barzel, B. & Barabási, A.-L. Network link prediction by global silencing of indirect correlations. *Nat. Biotechnol.* **31**, 720–725 (2013).
16. Harush, U. & Barzel, B. Dynamic patterns of information flow in complex networks. *Nat. Commun.* **8**, 2181 (2017).
17. Hens, C., Harush, U., Cohen, R., Haber, S. & Barzel, B. Spatiotemporal propagation of signals in complex networks. *Nat. Phys.* **15**, 403–412 (2019).
18. Barzel, B. & Biham, O. Binomial moment equations for stochastic reaction systems. *Phys. Rev. Lett.* **106**, 150602 (2011).
19. Pastor-Satorras, R., Castellano, C., Van Mieghem, P. & Vespignani, A. Epidemic processes in complex networks. *Rev. Mod. Phys.* **87**, 925–958 (2015).
20. Gardner, T. S., Cantor, C. R. & Collins, J. J. Construction of a genetic toggle switch in *Escherichia coli*. *Nature* **403**, 339–342 (2000).
21. Karlebach, G. & Shamir, R. Modelling and analysis of gene regulatory networks. *Nat. Rev. Mol. Cell Biol.* **9**, 770–780 (2008).
22. Holling, C. S. Some characteristics of simple types of predation and parasitism. *Can. Entomol.* **91**, 385–398 (1959).
23. Newman, M. E. J. *Networks—An Introduction* (Oxford Univ. Press, 2010).
24. May, R. M. Simple mathematical models with very complicated dynamics. *Nature* **261**, 459–467 (1976).
25. Strogatz, S. H. *Nonlinear Dynamics and Chaos with Student Solutions Manual: With Applications to Physics, Biology, Chemistry, and Engineering* (CRC Press, 2018).
26. Rual, J. F. et al. Towards a proteome-scale map of the human protein–protein interaction network. *Nature* **437**, 1173–1178 (2005).
27. Yu, H. et al. High-quality binary protein interaction map of the yeast interactome network. *Science* **322**, 104–110 (2008).
28. Robinson, P. K. Enzymes: principles and biotechnological applications. *Essays Biochem.* **59**, 1–41 (2015).
29. Wilson, H. R. & Cowan, J. D. Excitatory and inhibitory interactions in localized populations of model neurons. *Biophys. J.* **12**, 1–24 (1972).
30. Wilson, H. R. & Cowan, J. D. A mathematical theory of the functional dynamics of cortical and thalamic nervous tissue. *Kybernetik* **13**, 55–80 (1973).
31. Laurence, E., Doyon, N., Dubé, L. J. & Desrosiers, P. Spectral dimension reduction of complex dynamical networks. *Phys. Rev. X* **9**, 011042 (2019).
32. Gould, A. L. et al. Microbiome interactions shape host fitness. *Proc. Natl Acad. Sci. USA* **115**, E11951–E11960 (2018).
33. García-Bayona, L. & Comstock, L. E. Bacterial antagonism in host-associated microbial communities. *Science* **361**, eaat2456 (2018).
34. Willing, B. P., Russell, S. L. & Finlay, B. B. Shifting the balance: antibiotic effects on host–microbiota mutualism. *Nat. Rev. Microbiol.* **9**, 233–243 (2011).
35. Lim, R. et al. Large-scale metabolic interaction network of the mouse and human gut microbiota. *Sci. Data* **7**, 204 (2020).
36. Kehe, J., Ortiz, A., Kulesa, A., Gore, J., Blainey, P. C. & Friedman, J. Positive interactions are common among culturable bacteria. *Sci. Adv.* **7**, eabi7159 (2021).
37. Levy, R. & Borenstein, E. Metabolic modeling of species interaction in the human microbiome elucidates community-level assembly rules. *Proc. Natl Acad. Sci. USA* **110**, 12804–12809 (2013).
38. Allee, W. C., Park, O., Emerson, A. E., Park, T. & Schmidt, K. P. *Principles of Animal Ecology* (W. B. Saunders, 1949).
39. Costello, E. K., Stagaman, K., Dethlefsen, L., Bohannan, B. J. & Relman, D. A. The application of ecological theory toward an understanding of the human microbiome. *Science* **336**, 1255–1262 (2012).
40. Hsu, B. B. et al. Dynamic modulation of the gut microbiota and metabolome by bacteriophages in a mouse model. *Cell Host Microbe* **25**, 803–814 (2019).
41. ElHage, R., Hernandez-Sanabria, E. & Van de Wiele, T. Emerging trends in 'smart probiotics': functional consideration for the development of novel health and industrial applications. *Front. Microbiol.* **8**, 1889 (2017).
42. Liu, Y. Y. & Barabási, A.-L. Control principles of complex systems. *Rev. Mod. Phys.* **88**, 035006 (2016).
43. Isidori, A., Sontag, E. D. and Thoma, M. *Nonlinear Control Systems* Vol. 3 (Springer, 1995).
44. Hermann, R. & Krener, A. Nonlinear controllability and observability. *IEEE Trans. Autom. Control* **22**, 728–740 (1977).
45. Whalen, A. J., Brennan, S. N., Sauer, T. D. & Schiff, S. J. Observability and controllability of nonlinear networks: the role of symmetry. *Phys. Rev. X* **5**, 011005 (2015).
46. Coron, J.-M. *Control and Nonlinearity* (American Mathematical Society, 2007).
47. Sontag, E. D. *Mathematical Control Theory* (Springer, 1998).

Methods

Recoverability of modular networks. Applying our formalism to an empirically constructed brain network[48] allows us to examine its predictive power beyond our analytical assumptions of a random A. Indeed, the brain—with its two hemispheres—provides a highly structured (non-random) modular network, partitioned into two clearly distinctive communities $\mathcal{M}_1$ and $\mathcal{M}_2$ (Fig. 5f). It, therefore, offers meaningful insights into recoverability across modules. The question is can reigniting one module, say $\mathcal{M}_1$, spill over to also revive $\mathcal{M}_2$. Our analysis indicates that this depends on the average strength of the links within the modules, ω_{Intra}, versus that of the links between the two modules, ω_{Inter} (Fig. 5g). Clearly, if ω_{Intra} is too small, then both $\mathcal{M}_1$ and $\mathcal{M}_2$ are—in and of themselves—unrecoverable, and reigniting will inevitably fail (Fig. 5h). If both ω_{Intra} and ω_{Inter} are sufficiently large, then the reactivated nodes at $\mathcal{M}_1$ will further reignite their neighbours at $\mathcal{M}_2$, allowing a complete recovery of both modules via single-node reigniting (Fig. 5j). In between these two extremes, we observe a third phase in which reigniting is confined to $\mathcal{M}_1$ but fails to penetrate $\mathcal{M}_2$ (Fig. 5i).

The result is a three-state phase space (Fig. 5g): recoverable (blue) in which reigniting at $\mathcal{M}_1$ can reactivate also $\mathcal{M}_2$; unrecoverable (yellow) in which both modules cannot be revived; and modular (green) where $\mathcal{M}_1$ recovers but the reigniting signal fails to penetrate $\mathcal{M}_2$. To construct the phase diagram shown in Fig. 5g, we simulated neuronal dynamics on the brain network shown in Fig. 5f, scanning 2,500 distinct combinations of ω_{Intra} and ω_{Inter}. For each combination, we attempted 20 independent realizations of reigniting with randomly selected nodes. We then extracted η as the average number of revived modules over the 20 attempts. Hence, $\eta=0$ means that no module was revived (yellow) and $\eta=1$ indicates that (on average) reigniting was restricted to only the source node's module (green), but did not cross over to the other module. Finally, if $\eta=2$, then both modules were reactivated (blue).

This observation highlights the potential benefits of network modularity for self-recovery. Indeed, if one module fails, say $\mathcal{M}_2$, the other module, $\mathcal{M}_1$, if still active, can revive it. This is because $\mathcal{M}_1$'s active nodes can themselves help reignite the inactive $\mathcal{M}_2$. Hence, modularity offers a fail-safe network architecture in which, unless both modules simultaneously fail, one module can reactivate the other. This ensures sustained activity in the face of sporadic failures. To observe this, we simulated neuronal dynamics on our brain network, setting the intermodular link weights to $\omega_{\text{Inter}}=2$. Starting at $\mathbf{x}_1$, we introduce external noise that causes the activity of both modules to fluctuate, until a sufficiently large perturbation (randomly occurring at around $t\approx 20$) leads $\mathcal{M}_1$ to irreversibly fail (Fig. 5k, blue). Shortly after, a similar fate meets $\mathcal{M}_2$ (red) and the entire system collapses to $\mathbf{x}_0$.

We now repeat the exact same experiment but with $\omega_{\text{Inter}}=5$, bringing the system into the fully recoverable phase ($\eta=2$; Fig. 5l, blue). Now, at every instance in which, say $\mathcal{M}_1$ fails, $\mathcal{M}_2$'s active nodes reignite it back into activity (Fig. 5l). Hence, modularity can afford the system a fail-safe dynamics driven by its capacity for self-recoverability.

Selective reigniting in the microbiome. A unique aspect of our empirically constructed microbiome network is that it significantly deviates from a random topology. Indeed, in a random network, as degree correlations are negligible, the statistical properties of the shells $K_s(l)$ become approximately independent of s for $l>1$. In simple terms, although nodes may have diverse degrees, that is, $K_s(1)\neq K_{s'}(1)$, their second or third neighbours at $K_s(l>1)$ are statistically similar. Under these conditions, once a system is in the recoverable phase, one can reignite it using any desired node, as, indeed, all the nodes have roughly identical shells in their surrounding. If, however, the environments $K_s(l)$ vary significantly across the nodes, we expect that certain nodes become better reigniters than others. This gives rise to selective reigniting in which the system's recoverability is not only a function of the network but also depends on the specific source node s and its unique reigniting capacity.

Consider the reigniting signal as it propagates from source s and penetrates through the shells $K_s(1)$, $K_s(2)$,…. At a certain instance, it revives a node $i\in K_s(l)$ and then advances from i to impact its neighbour $j\in K_s(l+1)$ and so on (Fig. 6g). In Supplementary Section 3.3.3, we show that such propagation across shells, where a revived i can indeed reactivate its more distant neighbour j, requires that the $i\rightarrow j$ link weight exceeds a threshold w_0. Hence, links with weight $W_{ij}\geq w_0$ constitute effectual links that help propagate the reigniting signal. The remaining links with $W_{ij}<w_0$ have but a marginal contribution to the reigniting. We, therefore, construct an effective network comprising only the effectual links (Fig. 6h, blue links/nodes). This more selective network represents the relevant set of interactions that actively participate in the reigniting process. By constructing this network, we obtain the effectual shells surrounding each node s, whose number of nodes captures s's reigniting capacity $\mathcal{R}_s$. Nodes with large $\mathcal{R}_s$ are surrounded by many effectual links, and therefore, they have a higher reigniting capacity.

In a random topology, where all the shells are statistically similar, we expect minor differences in $\mathcal{R}_s$ between the nodes. In the microbiome, however, we find that $\mathcal{R}_s$ is highly diverse, with the top 26 species having $\mathcal{R}_s>300$, and the remaining species with $\mathcal{R}_s$ that is one or two orders of magnitude lower (Fig. 6i). Such diversity—a consequence of the unique structure of the microbiome—indicates that in this system, the top 26 nodes represent the preferred candidates for reigniting. To examine this, Supplementary Fig. 7 shows η versus the $\mathcal{R}_s$ ranking for all the nodes in the microbiome. We clearly observe that the top-ranked nodes have a much higher probability to successfully reignite the system.

Data availability

Empirical data required for constructing the real-world networks (Microbiome, Brain, Yeast PPI, Human PPI) are available at https://github.com/hillel26/NaturePhys2021.

Code availability

All codes to reproduce, examine and improve our proposed analysis are available at https://github.com/hillel26/NaturePhys2021.

References

48. Bullmore, E. & Sporns, O. Complex brain networks: graph theoretical analysis of structural and functional systems. *Nat. Rev. Neurosci.* **10**, 186–198 (2009).

Acknowledgements

H.S. acknowledges the support of the Presidential Fellowship of Bar-Ilan University, Israel, and the Mordecai and Monique Katz Graduate Fellowship Program. This research was supported by the Israel Science Foundation (grant nos. 499/19 and 189/19), the US National Science Foundation CRISP award (grant no. 1735505), the Bar-Ilan University Data Science Institute grant for research on network dynamics, the ISF-NSFC joint research program (grant nos. 3132/19 and 3552/21), the US–Israel NSF–BSF programme (grant no. 2019740), the EU H2020 project RISE (grant no. 821115), the EU H2020 project DIT4TRAM (grant no. 953783), the Defense Threat Reduction Agency (DTRA grant no. HDTRA-1-19-1-0016), the US National Science Foundation (grant no. 2047488) and the Rensselaer-IBM AI Research Collaboration.

Author contributions

All the authors designed the research. H.S. and B.B. conducted the mathematical analysis. H.S. performed the numerical simulations and analysed the data. A.B. supervised the microbiome analysis. B.B. was the lead writer of the paper.

Competing interests

The authors declare no competing interests.

Additional information

Supplementary information The online version contains supplementary material available at https://doi.org/10.1038/s41567-021-01474-y.

Correspondence and requests for materials should be addressed to Baruch Barzel.

Peer review information *Nature Physics* thanks Patrick Desrosiers and the other, anonymous, reviewer(s) for their contribution to the peer review of this work.